

# Hybrid based on Phenazine Conjugated Microporous Polymer as a High-Performance Organic Electrode in Aqueous Electrolytes

Diego Alván<sup>+</sup><sup>[a]</sup>, Rebecca Grieco<sup>+</sup><sup>[a]</sup>, Nagaraj Patil,<sup>\*[a]</sup> Andreas Mavrandonakis,<sup>[a]</sup> Marta Liras,<sup>[b]</sup> and Rebeca Marcilla<sup>\*[a]</sup>

Incorporating redox active units in a 3D porous network is an encouraging strategy to enhance electrochemical performance of organic electrode materials. Herein, a new hybrid composed by phenazine-based conjugated microporous polymer (IEP-27-SR, stand for IMDEA Energy Polymer number 27) and single-walled carbon nanotubes (SWCNTs) and graphene oxide (RGO) is synthesized, fully characterized and tested electrochemically in different aqueous electrolyte conditions, i.e., at various pH values (1–12) and also with different charge carriers ( $H^+$  in acidic, and  $Li^+$ ,  $Na^+$ ,  $K^+$  in neutral and alkaline electrolytes).

Although the IEP-27-SR is found to be very versatile showing very good electrochemistry both in alkaline and acidic solution, it exhibits best specific capacity, redox kinetics and cycle stability in acidic electrolyte. Then encouragingly, when IEP-27-SR is combined with an activated carbon (AC) counter electrode to construct a proof-of-the-concept device, the IEP-27-SR//AC demonstrates high specific capacity ( $168 \text{ mAhg}^{-1}$  at 2 C), impressive rate performance ( $96 \text{ mAhg}^{-1}$  at 60 C) and ultra-long cycle stability (76% capacity retention over 28800 cycles at 10 C; 2690 h) in 1 M  $H_2SO_4$ .

## Introduction

Nowadays, the growing energy demand is encouraging the development of low cost, environmentally friendly, sustainable energy storage devices.<sup>[1,2]</sup> In this context, it is very critical to design energy storage materials that are easy to synthesize, based on earth-abundant elements, cheap, chemically robust, environmental friendly and inexpensive. However, most of the electrode materials in current battery technologies dominated by inorganic compounds, that are mostly toxic and/or composed of scarce elements such as Pb, Ni, Co, Li, etc. This raises environment pollution, safety risk and concerns about future sustainable development.<sup>[3]</sup> Moreover, the redox mechanism of inorganic materials mostly consists of the insertion-deinsertion of ions that leads to structural deformation during the operation of the battery. This is especially important when insertion of high-charge dense and/or voluminous charge

carriers have place like in multivalent batteries.<sup>[4]</sup> For this reason, the most successful application of these intercalation compounds has been in organic lithium-ion batteries where  $Li^+$ , with small charge/radius ratio, is employed as charge carrier. However, on the positive side, the use of non-aqueous electrolytes in Li-ion batteries is beneficial for the development of high energy density batteries, but the safety and environmental disquiets due to their flammability, toxicity, high cost, and environmental unfriendliness are less promising from the sustainability and scalability point of view.<sup>[5–7]</sup>

Though historically developed first, and despite later overtaken by Li-ion battery market, interest in aqueous rechargeable batteries (ARBs) has been resurfacing in the recent years for the development of more sustainable energy storage systems.<sup>[8]</sup> ARBs offer significant advantages over Li-ion batteries in terms of safety and cost effectiveness due to the nonvolatility, nontoxicity, and nonflammability of water-based electrolytes.<sup>[9]</sup> Additionally, ARBs also bring the possibility of fast charging and high power densities due to the high ionic conductivity of aqueous media.<sup>[10]</sup> However, when applied in ARBs, intercalation inorganic electrodes such as manganese-based oxides, vanadium-based compounds or Prussian blue analogues do not show sufficiently good performance in terms of rate performance<sup>[11]</sup> and stability, undergoing volume and structural changes during the ions intercalation.<sup>[12]</sup> One of the most promising alternatives are organic electrode materials (OEMs). They are composed of naturally abundant elements, are inexpensive, environmental benign and characterized by high theoretical capacity and excellent structural versatility and synthetic flexibility.<sup>[13,14]</sup> Also, differently from inorganic intercalation materials, their redox mechanism consists on an “ion-coordination” that does not alter the chemical structure significantly, avoiding structural deformation and guarantying

[a] D. Alván,<sup>+</sup> R. Grieco,<sup>+</sup> Dr. N. Patil, Dr. A. Mavrandonakis, Dr. R. Marcilla  
Electrochemical Processes Unit,  
IMDEA Energy Institute  
Avda. Ramón de la Sagra 3, 28935 Móstoles (Spain)  
E-mail: nagaraj.patil@imdea.org  
rebeca.marcilla@imdea.org

[b] Dr. M. Liras  
Photoactivated Processes Unit,  
IMDEA Energy Institute  
Avda. Ramón de la Sagra 3, 28935 Móstoles (Spain)

[+] These authors contributed equally to this work.

 Supporting information for this article is available on the WWW under  
<https://doi.org/10.1002/batt.202300023>

 An invited contribution to a Special Collection on Organic Batteries

 © 2023 The Authors. *Batteries & Supercaps* published by Wiley-VCH GmbH.  
This is an open access article under the terms of the Creative Commons Attribution License, which permits use, distribution and reproduction in any medium, provided the original work is properly cited.

the stability of the electrode while cycling. Moreover, organic electrodes are versatile materials endowing the reversible coordination/uncoordination of both mono- ( $\text{Li}^+$ ,  $\text{Na}^+$ ,  $\text{K}^+$ ) and even multivalent ions ( $\text{Zn}^{2+}$ ,  $\text{Mg}^{2+}$ ,  $\text{Al}^{3+}$ ) which make them interesting candidates for different type of ARBs.<sup>[15,16]</sup> Until now, various redox organic materials such as nitroxide radicals,<sup>[17]</sup> carbonyls,<sup>[18]</sup> and pyrazine heterocyclic aromatics<sup>[19]</sup> have been applied as electrodes in ARBs, but mostly in neutral aqueous metal-ion configurations. In these battery configurations OEMs have demonstrated modest rate performance and power capability due to the moderate performance of metallic ions as charge carriers. Differently from neutral electrolytes, acid electrolytes with higher ionic conductivity guarantee faster kinetics in the host structures and better rate performance. This is due to the lightest mass and smallest ionic radius of non-metallic protons that move rapidly along the hydrogen-bonding network thanks to a Grotthuss conduction mechanism.<sup>[20]</sup> Similar to acidic electrolytes, alkaline electrolytes can also offer high ionic conductivity (0.6 S cm<sup>-1</sup> for 6 M KOH at 25 °C) that improves the rate performance compared to the neutral electrolytes.<sup>[21]</sup> Moreover, alkaline electrolytes typically containing KOH (ranging from 1 to 6 M), are of particular interest for some battery applications (e.g., metal-air,<sup>[22-24]</sup> Zn–Ni,<sup>[25]</sup> metal hydride–Ni,<sup>[26,27]</sup> etc.).

To date, the number of organic materials that stably operate in acidic conditions, is further limited to quinones and pyrazines.<sup>[18,28-45]</sup> Although most of these small molecules and their linear polymer analogues showed high value of initial capacity, they still suffer from complete or partial dissolution into the electrolyte, resulting in poor cycling stability. In the particular case of phenazine-based compounds, their  $\pi$ -conjugated aromatic structure containing N heteroatoms with a lone pair of electrons attracted the interest of the scientific community. Phenazine active unit shows a lower redox potential (~0.2 V vs. NHE in 1 M H<sub>2</sub>SO<sub>4</sub>)<sup>[29]</sup> and a proton-storage capability that makes it as a suitable anode in proton-based batteries.<sup>[46]</sup> Recently, Minjie Shi et al.<sup>[29]</sup> demonstrated an improved proton-storage capability of a rod-like diquinoxalinophenazine (DPZ) compared to the phenazine monomer (PZ) in a 1 M H<sub>2</sub>SO<sub>4</sub> owing to the enhanced structural stability of the DPZ, sustaining 300 cycles at 3 C, whereas the phenazine small molecule dissolved after 100 cycles. Another promising strategy to increase the structural stability of redox organic compounds is to develop conjugated (micro)porous polymers (C(M or P)Ps) and covalent organic framework (COFs).<sup>[47]</sup> Benefiting from their large specific surface area, delocalized  $\pi$ -conjugated skeleton, combination of micro-/mesoporosity, etc. high active material utilization, particularly at high mass loading and in high polymer content electrodes, along with fast charging capability and high-power are demonstrated.<sup>[24,48-50]</sup> Moreover, due to the robustness of the polymer backbone and mechanically stable 3D microporous structure, they are fully insoluble and have recently emerged as ideal candidates for long-lived batteries.<sup>[24,50]</sup> However, only a few examples of porous polymers containing mostly quinone derivatives have been investigated in acidic electrolytes.<sup>[39-45]</sup>

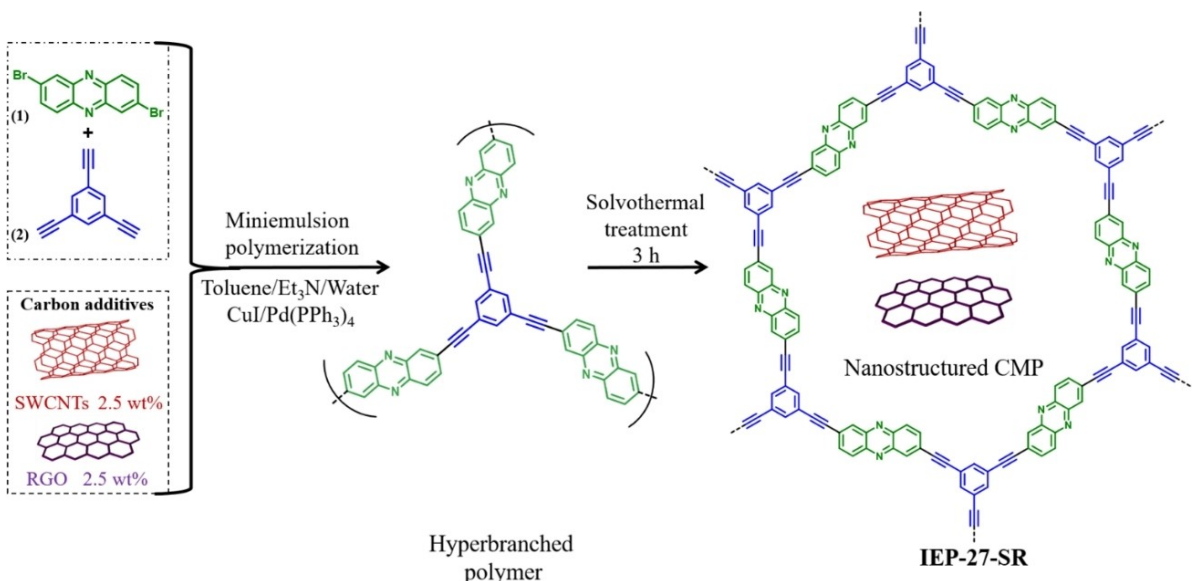
Considering the fast kinetic of acidic electrolytes (i.e., H<sub>2</sub>SO<sub>4</sub>) and the proton storage properties of azaacene active unit, here we selected phenazine building block and incorporate it in a porous framework (named IEP-27, IEP stands for IMDEA Energy Polymer) with the aim of solving the dissolution issue faced by the organic small molecules. Furthermore, here we designed a hybrid which comprising small amounts of single-walled carbon nanotubes (SWCNTs) and reduced graphene oxide (RGO) (ca. 3.5 + 3.5 wt.%) following our previous knowledge.<sup>[51]</sup> Inclusion of carbons during the synthesis enables the fabrication of self-supported binder- and metal collector-free high active-material content (ca. 80 wt.%) electrodes called buckypapers with enhanced intrinsic electrochemical characteristics of the porous polymer, but without compromising its electrochemical performance. This new hybrid phenazine-based conjugated porous polymer (named IEP-27-SR; S from SWCNTs and R from RGO) was synthesized and fully characterized to confirm its porous microstructure before performing its complete electrochemical characterization in different aqueous electrolytes including basic, neutral and acidic pH. To the best of our knowledge, this is the first time that a *n*-type phenazine unit is incorporated in a porous amorphous backbone, specifically as a CMP (not to be confused with covalent organic frameworks, that are crystalline), and applied as electrode in alkaline and acidic electrolytes.

## Results and Discussion

### Synthesis and characterization of hybrid phenazine-based porous polymer (IEP-27-SR)

The new hybrid phenazine-based conjugated porous polymer (named IEP-27-SR) was synthesized applying a protocol previously developed by us.<sup>[49,51]</sup> This protocol consists in a Sonogashira cross-coupling reaction that combines a miniemulsion polymerization followed by a solvothermal treatment and including carbon additives during the synthesis. Specifically, in this work, the IEP-27-SR was synthesized as shown in Scheme 1, by reacting 2,7-dibromophenazine (1) and 1,3,5-triethylbenzene (2) via a Sonogashira cross-coupling reaction and including carbon additives (2.5 wt.% of single-walled carbon nanotubes (SWCNTs) and 2.5 wt.% of reduced graphene oxide (RGO)) during the synthesis. The 2,7-dibromophenazine (1) was synthesized modifying a protocol already published<sup>[52]</sup> and more details are given in Supporting Information.

Chemical composition of IEP-27-SR was determined by solid-state <sup>13</sup>C NMR spectroscopy and Fourier transform infrared spectroscopy (FTIR) (Figure 1a, b) which can confirm the success of the polymerization process. Solid-state <sup>13</sup>C NMR confirms the presence of the C=N signal (imine group) at 142 ppm that belongs to the phenazine active units while the peaks around 123–129 ppm correspond to C=C from aromatic rings present in both the building blocks. Furthermore, at 90 ppm appears a peak conforming to the –C≡C– attributed to the linker which confirms the successful cross-coupling Sonogashira reaction. The absence of a HC≡C– peak corresponding to



Scheme 1. Synthetic scheme for the preparation of hybrid IEP-27-SR showing its idealized chemical structure.

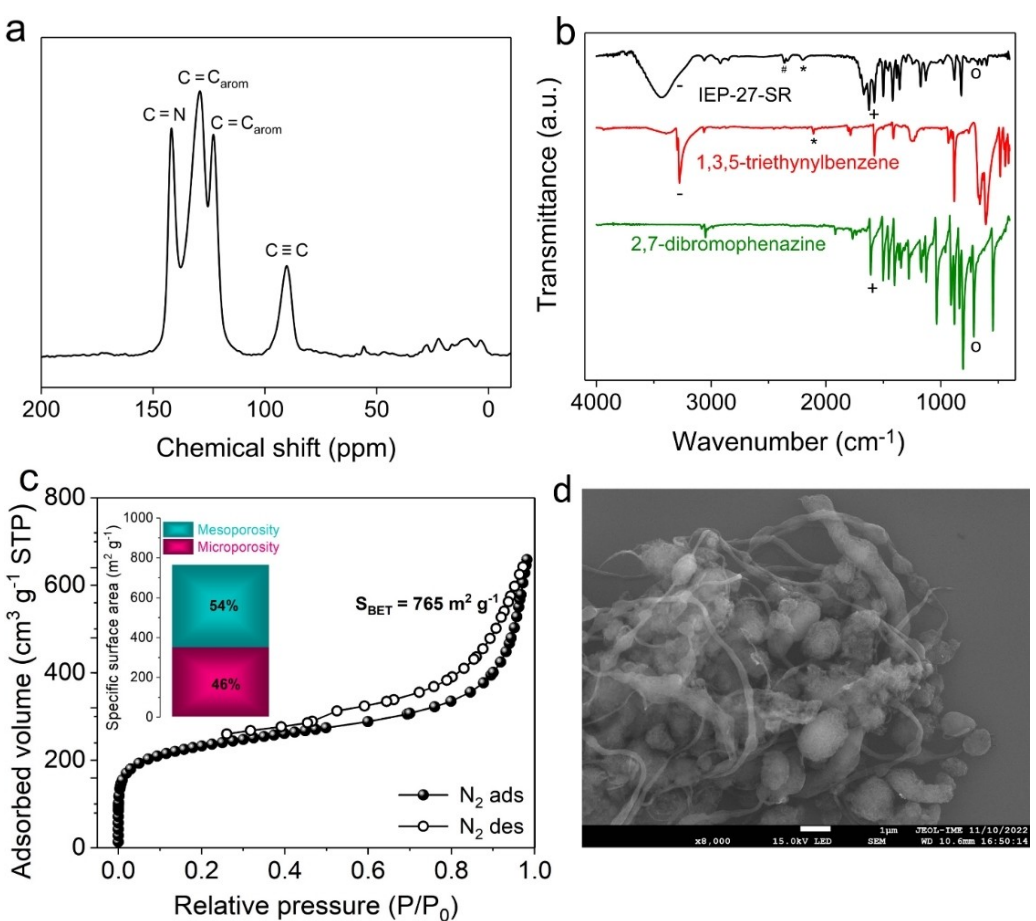


Figure 1. Physico-chemical characterization of IEP-27-SR. a)  $^{13}\text{C}$  NMR, b) FTIR (Legends are -:  $\text{C}\equiv\text{C}-\text{H}$ , #:  $\text{CO}_2$  ambiental, \*:  $\text{C}\equiv\text{C}$ , +:  $\text{C}=\text{N}$ , o:  $\text{C}-\text{Br}$ ), c) nitrogen adsorption-desorption isotherm profile with percentages of micro-/mesoporosity in inset, and d) SEM picture at  $\times 8,000$ , 15.0 kV.

the starting material, 1,3,5-triethynylbenzene which appears ca. 75 ppm, further attests its incorporation to build network backbone. The FTIR of IEP-27-SR exhibits a  $\text{C}=\text{N}$  stretching

vibration at  $1623 \text{ cm}^{-1}$  that is also present in the 2,7-dibromophenazine building block. The appearance of peak at  $2202 \text{ cm}^{-1}$  resulting from the triple bond intermediate  $\text{C}\equiv\text{C}$ ,

indicates the loss of the alkyne protons, and the subsequent connection with the 2,7-dibromophenazine. Furthermore, the absence of the peaks at 715 and 1032 cm<sup>-1</sup> in the polymer spectrum proves the disappearance of the C–Br bond. Textural properties of the hybrid porous polymer were investigated by nitrogen adsorption-desorption analysis as presented in Figure 1(c). The isotherm exhibits a type IV, typical of mesoporous materials and characterized by a Type H2(b) hysteresis loop. The extracted and calculated textural parameters from the isotherms are collected in Table S1. Specific surface area ( $S_{BET}$ ) was calculated to be 765 m<sup>2</sup> g<sup>-1</sup> with microporous and mesoporous surface fractions of 46% and 54%, respectively (Figure 1c, inset). Pore size distribution was obtained from the quenched solid density functional theory (QSDFT) model and further confirms that the IEP-27-SR is defined by the presence of both the types of porosities (micro and meso; Figure S3).

Amorphous nature of the porous polymer was confirmed by powder X-ray diffraction measurements (Figure S4a). The morphology of the polymer particles was characterized by Scanning electron microscope (SEM, Figure 1d) and by transmission electron microscopy (TEM, Figure S4c, d). Figure 1d shows round-shape nanoparticles combined with long porous nanowires, resembling spaghetti like nanostructure.<sup>[51]</sup> From TEM images, we could estimate an average particles round-shape diameter of 300–400 nm, clearly characterized by a porous nature (Figure S4c). The synergistic inclusion of the carbon additives is also evident as the SWCNTs (wire shape) and RGO (crystalline structure) envelop the polymer particles. Finally, the microanalysis and elements mapping clearly show the presence of C, O and N, which are homogeneously distributed in all the sample (Figure S3b).

#### pH-Dependent electrochemical characterization of IEP-27-SR using buffered electrolytes

The electrochemical properties of the IEP-27-SR were first characterized in a series of Britton-Robinson aqueous universal buffer solutions to evaluate its pH-dependency, as the pH values of the electrolyte are expected to significantly influence the electrochemical performances. The buffer solutions were

prepared to increase gradually the pH, considering a pH range between 1.1–12 and cyclic voltammograms were recorded using an IEP-27-SR-modified glassy carbon as working electrode (Figures 2a, b and S5). The voltammogram obtained in the pH=1.1 exhibited a single reduction and oxidation peak at -76 (vs. Ag/AgCl) and 20 mV, respectively, with a potential peak-to-peak separation of 56 mV. In the pH range 1.1 < pH < 5.5 (mild acidic conditions), the peak potentials shifted negatively with increasing pH. Plot of  $E_{1/2}$  versus solution pH (Figure 2c) presented a linear trend with a slope of ~58 mV/pH unit increment, close to the 59 mV/pH unit expected for proton coupled redox reactions with a one-to-one stoichiometry between electrons ( $n$ ) and protons ( $m$ ), based on the Nernst equation:<sup>[53]</sup>

$$\begin{aligned} E &= E^0 + \frac{0.059}{n} \log \frac{[\text{phz}]_{\text{ox}} [\text{H}^+]^m}{[\text{phz}]_{\text{re}}} \\ &= (E^0 + \frac{0.059}{n} \log \frac{[\text{phz}]_{\text{ox}}}{[\text{phz}]_{\text{re}}}) - \frac{0.059 \times m}{n} \text{pH(V)} \\ &= E^0 - \frac{0.059 \times m}{n} \text{pH(V)} \end{aligned} \quad (1)$$

The redox mechanism of phenazines in acidic conditions was further confirmed by FTIR analysis of the pristine sample and the reduced and oxidized sample in 1 M H<sub>2</sub>SO<sub>4</sub>. Figure S6 shows the concomitant appearance of a new peak at 1300 ppm associated to the C–N bond, formed during the reduction of the phenazine, while the peak corresponding to C=N, clearly visible at 1590 ppm in the pristine electrode, almost disappears. Oxidized sample resembles pristine electrode with an evident signal 1590 ppm for the C=N whereas the peak at 1300 ppm associated to the C–N bond disappears.

Furthermore, when the pH was 5.5, IEP-27-SR exhibited broad oxidation and reduction peaks, and the CV features emerged from single redox pair in mild acidic conditions to less discernible two separate peaks presumably (Figure S5b). In the pH range 7 < pH < 10 (neutral-to-mild alkaline conditions), reduction peaks became weak, and multiple corresponding reoxidations peaks were identified with larger redox peak separation. Moreover,  $E_{1/2}$  versus solution pH in this pH range presented a slope of ~36 mV/pH unit increment (Figure 2c),

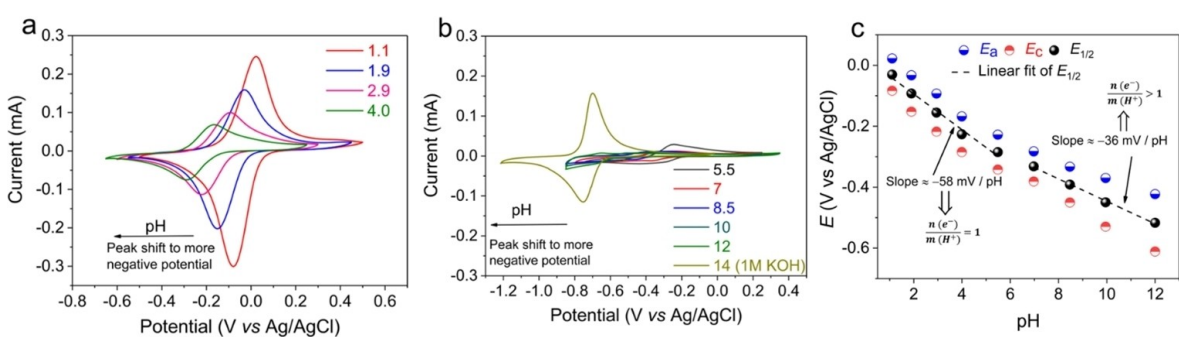


**Figure 2.** Electrochemistry of IEP-27-SR in a series of Britton-Robinson universal aqueous buffer solutions, pH = 1.1–12, evaluated in the three-electrode configuration. a) CVs at 5 mVs<sup>-1</sup> at different pH (1.1 < pH < 4), b) CVs at 5 mVs<sup>-1</sup> at different pH (5.5 < pH < 12), including pH 14 (1 M KOH), and c) linear correlation between the redox peak position and the formal potential on the pH.

suggesting that less protons involvement than the one-to-one stoichiometry between electrons and protons observed in mild acidic conditions (58 mV/pH). Interestingly at pH 14 (1 M KOH), further increase in the intensity of redox peaks, along with decreased polarization and enhanced reversibility was noticed (Figure S5c). These differences in the electrochemical energy storage mechanisms at different pH regimes, might be attributed to the competitive electroneutralization reaction of  $H^+$  and  $M^+$  on the electronegative N atom in phenazine.<sup>[53,54]</sup>

It is also worth to mention here that the CV peak currents of IEP-27-SR greatly decreased with the increase of pH until pH 7, with concomitant decrease of specific capacity (Figure S7). One of the possible reasons for this is due to the less available  $H^+$  that leads to a decrement in the apparent rate of charge transport in the electrode at higher pH values. We carried out scan rate dependence of CVs at two representative pH conditions, i.e., pH 1.1 and pH 4.4, to clarify the accounted mass-transfer limited process (Figure S8a and b). As shown in Figure S8(c), specific capacity decreased with increase of scan rates at both the pHs, but the decrease was slightly faster at the higher pH of 4.4, suggesting better rate capability at pH 1.1 (Figure S8d). Noteworthily, IEP-27-SR achieved 91.3 mAh g<sup>-1</sup> (for instance, at 5 mVs<sup>-1</sup>) at pH 1.1, however similar specific capacity was obtained but at a 5-fold slower scan rate of 1 mVs<sup>-1</sup> at pH 4.4. Also, at a sufficient slow scan rate of 0.25 mVs<sup>-1</sup>, a high value of 112 mAh g<sup>-1</sup> was obtained at pH 4.4, that is about 70% compared to the highest specific capacity reached at the same scan rate in pH 1.1. These experiments partially confirm limitations of mass-transfer at high scan rates, particularly in less protic conditions within proton-coupled redox process range.

Furthermore, similar specific capacities attained in neutral-to-mild basic conditions, and increase in its value at pH 14 (Figure S7), once again suggests that redox mechanism of phenazine is not fully proton coupled in these conditions, and might involve metal cation charge carriers.

In order to gain insights on the reduction mechanism of phenazine with  $2H^{+}/2e^-$  or  $M^{+}/2e^-$  ( $M^+ = Li, Na, K$ ), we made use of quantum-chemical calculations based on density functional (DFT) and accurate DLPNO-CCSD(T) wave function theory (WFT). The concentration effect of protons or potassium cations is also considered by adding the term  $RT\ln\frac{Q'}{Q}$  to the reduction free energies. In this term,  $Q$  is the reaction quotient (i.e., the ratio of concentrations that appear in the equilibrium constant) evaluated with all species at their standard-state concentrations that are assumed to be 1 M. Full details of the calculations are given in the Supporting Information. The free energies ( $\Delta G$ ) for the  $2e^-/2H^+$  reduction of phenazine at three different representative pH values of 1, 4 and 7 were computed to be -206.9, -196.0 and -187.8 kcal/mol respectively, revealing more negative  $\Delta G$  value in the lowest pH conditions (Figure S9 and Table S3). This suggests that reduction of phenazine is thermodynamically favored in the solution containing highest proton activity.

The combined experimental and computation results reveal that strongly protic conditions favors the redox activity of

phenazine groups in terms of active-material utilization and kinetics that are also in good agreement with the observations made by Oyama et al.<sup>[55]</sup> and Sivakkumar et al.<sup>[56]</sup>

### Insights into the electrochemistry of IEP-27-SR in neutral and alkaline electrolytes

For a more realistic comparison of the phenazine redox behavior in different pH conditions, three different electrolytes at the same concentration (1 M of each  $H_2SO_4$ ,  $NaCl$ ,  $KOH$ ) were selected as representative acid, neutral and basic electrolytes, respectively. Figure 3 shows the voltammograms (potentials were converted to NHE) of the IEP-27-SR in these selected electrolytes. At the fixed scan rate of 5 mVs<sup>-1</sup>, a pair of reversible peaks around  $E_{pa}$  0.26/ $E_{pc}$  0.24 V, irreversible peaks around -0.6/-0.05 V and quasi-reversible peaks around -0.38/-0.47 V, corresponding to the oxidation/reduction reactions in acidic, neutral and basic electrolytes, respectively, were observed. The smallest peak separation of 40 mV, along with visibly the highest CV area, once again indicates that the IEP-27-SR exhibited highest redox activity in 1 M  $H_2SO_4$ . Additionally, as already pointed out before, poor redox activity with the highest peak polarization of >600 mV and smallest CV area were noted in 1 M  $NaCl$ . While in 1 M  $KOH$  a compromised redox behavior in terms of peak separation and CV area enclosed observed that is in between acidic and neutral electrolyte conditions. The electrochemical behavior of phenazine units in IEP-27-SR in the neutral and basic electrolytes is further discussed in detail in following paragraphs.

**Neutral electrolytes.** Neither by changing the type of charge carriers, i.e.,  $Li^+$ ,  $Na^+$ ,  $K^+$  (Figure S10a) nor by increasing concentration from 0.1 M to 5 M of  $Na^+$  as the representative charge carrier in the neutral medium (Figure S10b), significantly elevated its redox activity. We also assembled a representative device against AC, using a common and better neutral salt, i.e., 1 and 10 M LiTFSI, which either delivered significant capacities

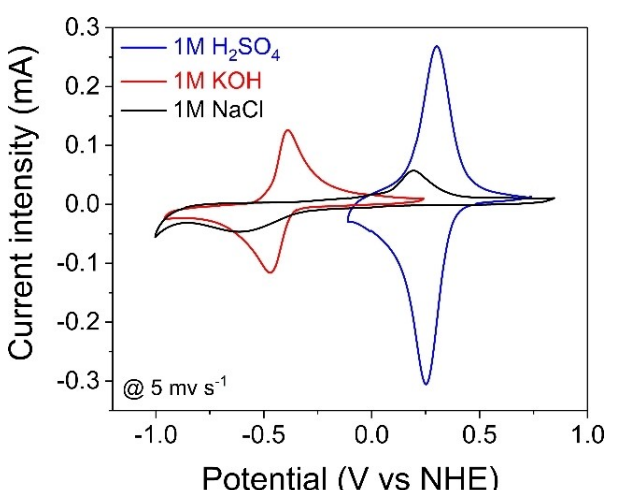


Figure 3. Representative CVs of IEP-27-SR at 5 mVs<sup>-1</sup> in 1 M of each acidic ( $H_2SO_4$ ), neutral ( $NaCl$ ) and basic ( $KOH$ ) aqueous electrolytes.

(typically below  $40 \text{ mAh g}^{-1}$  that is less than 20% of theoretical capacity), even at sufficient low C-rates of C/5 and C/2. (Figure S11). Li et al. comprehensively studied pH-dependent electroactivity of phenazine small molecule experimentally and supplemented by DFT calculations, and confirmed that the trace amounts of  $\text{H}^+$  in the electrolyte could coordinate with the electronegative N atom in phenazine spontaneously, and could affect its electrochemical performance.<sup>[54]</sup> We also found that the dependence of  $E_{1/2}$  on the concentration of electro-neutralizing  $\text{Na}^+$  in the neutral medium yielded slope of  $20 \text{ mV}/[\text{Na}^+]$ , which is lower than ideal  $59 \text{ mV}/[\text{Na}^+]$ , if one-to-one stoichiometry between electrons and  $\text{Na}^+$  is involved in the redox reactions (Figure S12 and related note).<sup>[57,58]</sup> This lower value of slope once again suggests mixed  $\text{H}^+$  and  $\text{Na}^+$  charge storage in the neutral electrolyte, as the concentration of  $\text{H}^+$  is not negligible, and the competitive electroneutralization reaction between  $\text{H}^+$  and  $\text{M}^+$  could lead to the high peak polarization along with poor capacities.<sup>[19,54]</sup>

**Alkaline electrolytes.** Then switching to alkaline aqueous electrolytes, first, the CV of IEP-27-SR in a typical three-electrode system was evaluated in a series of basic-pH solutions containing different charge carriers (1 M LiOH, 1 M NaOH, and 1 M KOH). As shown in Figure S13, a pair of reversible redox peaks around  $-0.6 \text{ V}$  (vs. Hg/HgO) can be recognized in all the alkaline electrolytes without much differences.<sup>[59]</sup> Second, by employing buckypaper electrodes with mass loading of

$2 \text{ mg cm}^{-2}$ , we studied rate and cycling performance of IEP-27-SR in 4 M of each LiOH, NaOH, and KOH to check if the cations in alkaline electrolyte affect the electrochemical performance. Analogous to the CV results, a similar average discharge potential around  $-0.61 \text{ V}$  (vs. Hg/HgO) was found in all these cases (Figure 4a-c). Additionally, slightly higher discharge capacities of  $138$  and  $130 \text{ mAh g}^{-1}$  at the lowest C-rate of 2 C were recorded in 4 M LiOH and KOH, respectively, compared to a lower  $114 \text{ mAh g}^{-1}$  in 4 M NaOH (Figure 4d). However, the trend in discharge capacity decay at various C-rates was also mostly identical, suggesting similar rate capability (Figure 4e). Moreover, upon cycling at 10 C over 200 cycles, the IEP-27-SR retained similar discharge capacity retentions around 94% in NaOH and KOH, with a marginally improved retention of 99% in LiOH (Figure 4f). These studies implied that different cations in the alkaline electrolyte do not affect the electrochemical performance of IEP-27-SR to the great extent.

Then, using KOH as the representative basic electrolyte, the potential dependence of IEP-27-SR on the concentration of KOH was evaluated. Differently to the quinones where above a certain pH the potential is pH-independent,<sup>[18,50,60]</sup> surprisingly the peak potentials of IEP-27-SR shifted to even more negative values when the KOH concentration increased from 1 to 10 M KOH, (Figure S14) suggesting still proton involvement in these basic conditions. Li et al. also reported similar findings – a more negative redox peak shift to lower potentials in 6 M KOH

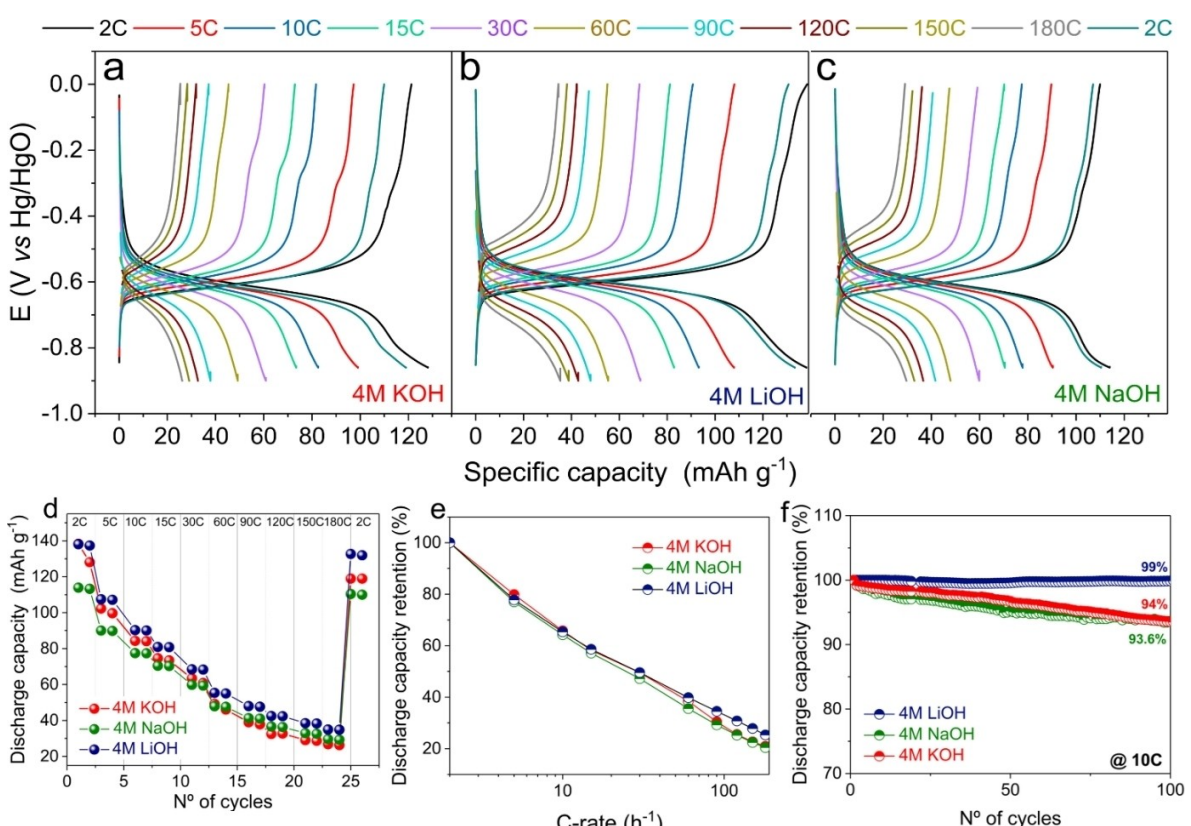


**Figure 4.** Electrochemical performance of IEP-27-SR buckypaper electrodes in 4 M alkaline electrolytes evaluated in 3 electrode. a–c) specific capacity-potential profiles in 4 M of each a) KOH, b) LiOH, c) NaOH at various C-rates; d) the corresponding discharge capacity vs. cycle number and e) discharge capacity retention rate at various C-rates, and f) cycle stability at 10 C.

compared to that in pH 13.5.<sup>[54]</sup> Once again, we computed  $\Delta G$  for the reduction of phenazine with  $2\text{H}^+/\text{2e}^-$  versus  $2\text{K}^+/\text{2e}^-$  in 1, 4 and 10 M KOH, revealing slightly more negative  $\Delta G$  values ( $\Delta G = -168.7$  vs.  $-161.1$ ,  $-166.0$  vs.  $-162.8$  and  $-164.7$  vs.  $-163.9$  kcal/mol, respectively), upon electroneutralization with  $\text{H}^+$ , corroborating the CV results. But it is worth to mention that the difference in  $\Delta G$  for the reduction with  $\text{H}^+$  vs  $\text{K}^+$  became smaller with the increase of KOH concentration, for instance only 0.8, 3.2, and 7.6 kcal/mol at 10, 4 and 1 M KOH, respectively (Figure S15). And furthermore, these energy differences are significantly smaller than the  $\Delta G$  differences, for instance, at pH 1 (44.1 kcal/mol) (Table S3 and Figure S15). These minimum energy differences in alkaline conditions suggest the competitive binding of  $\text{H}^+$  and  $\text{K}^+$  charge carriers with phenazine moieties, and do not favor the selective reduction with only  $\text{K}^+$  over  $\text{H}^+$  charge carriers, but most probably dominated by  $\text{K}^+$  storage. This statement is supported by the observed evidence of drastically reduced CV peak polarizations, along with significantly augmented specific capacity values in the alkaline media, close to the capacities in acidic conditions (discussed in the next section) compared to the neutral media.

Based on our findings and previous literature reports, therefore we can conclude that the reduction of phenazine is proton-coupled in acidic conditions, and most probably accompanied by binding with  $\text{H}^+$  and/or  $\text{M}^+$  charge carriers, but dominated by  $\text{H}^+$  and  $\text{M}^+$  storage in neutral and alkaline conditions, respectively.

## Redox kinetics and rate capability studies in acidic (1 M $\text{H}_2\text{SO}_4$ ) and alkaline electrolytes (5 M KOH)

We selected acidic (1 M  $\text{H}_2\text{SO}_4$ ) and basic conditions (5 M KOH) to further evaluate the electrochemical performance of IEP-27-SR in detail.

CV experiments at various scan rates (from 0.1 to 100 mV s<sup>-1</sup>) were carried out on buckypaper electrode (2 mg cm<sup>-2</sup> polymer mass loading) using a three-electrode setup in 1 M  $\text{H}_2\text{SO}_4$  (pH ≈ 0) (Figure 5a). The Laviron method was used to determine transfer coefficient ( $\alpha$ ) and heterogeneous reaction rate constant ( $k^0$ ), fundamental parameters for estimating the reversibility and kinetics of the redox system (Figure 5b). When the scan rate increases from 0.1 to 100 mV s<sup>-1</sup>, the  $\Delta E_p$  expands consequently (as normally observed for battery-type materials); however, the CVs appear to be characterized by a small peak-to-peak potential separation, indicating a fast kinetic.<sup>[61]</sup> The  $\alpha$  was calculated to be 0.45, close to 0.5, demonstrating a good symmetry of the electron transfer energy barrier of the redox reactions, while  $k^0$  was determined to be 0.4 s<sup>-1</sup>, significantly a high value for a battery-type practical electrode.<sup>[50]</sup> Furthermore, power-law analyses of peak currents ( $i_p$ ) as a function of the scan rate ( $v$ ) were further extrapolated from the CV plots, since the  $i_p$  in the CV curves as a function of the  $v$  obeys to this law:  $i_p = av^b$  where,  $a$  and  $b$  are adjustable coefficients<sup>[62]</sup> (Figure 5c). The exponential b-value parameter was determined from the slope of the linear plot of  $\log i_p$  versus  $\log v$  and is used to describe the electrode kinetics. When  $b=1$ , the electrode exhibits a characteristic of capacitive-controlled behavior while a b-value of 0.5 indicates a diffusion-controlled process. The b-value was found to be 0.95/1 (anodic/cathodic) in 1 M  $\text{H}_2\text{SO}_4$  indicating an

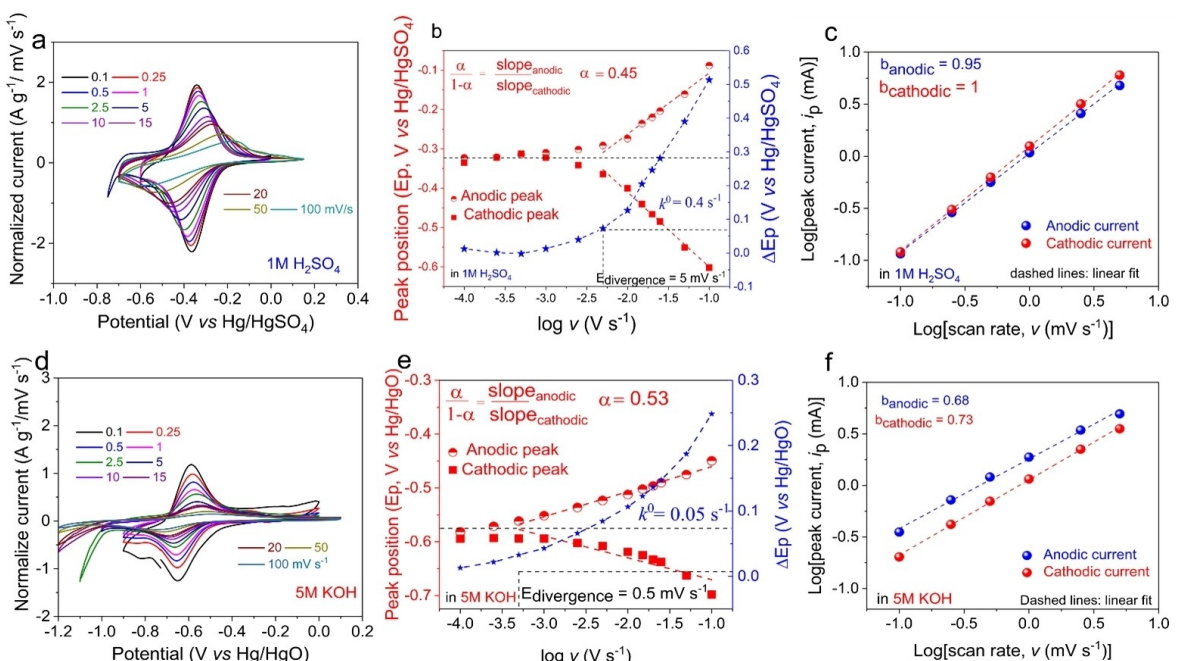


**Figure 5.** Redox kinetics analysis of IEP-27-SR buckypaper electrodes: (a, d) CVs (scan rate-dependency), (b, e) the corresponding Laviron plots, and plot of peak current vs scan rate in logarithmic scale to obtain b-values according to  $i_p = av^b$  in 1 M  $\text{H}_2\text{SO}_4$  (a–c) and 5 M KOH (d–f).

extremely fast redox processes characterized by a capacitive-controlled behavior in the acidic electrolyte.

The kinetics parameters  $\alpha$  and  $k^0$  were calculated to be  $\alpha = 0.53$  and  $k^0 = 0.05 \text{ s}^{-1}$  in 5 M KOH (Figure 5d, e). The  $k^0$  in 5 M KOH was 8-fold smaller than that in 1 M H<sub>2</sub>SO<sub>4</sub>, indicating a faster kinetics in the acidic electrolyte. Moreover, the  $b$ -value was found to be 0.68/0.73 (anodic/cathodic) in the 5 M KOH electrolyte, indicating a more diffusion-limited redox processes in the basic electrolyte compared with the acidic one.

On account of diminished redox kinetics parameters in alkaline electrolyte compared to acidic electrolyte, a relatively faster decrease in CV area (Figure 5a, d) and corresponding decrease in the specific capacity (Figures 5a, d, and S16a), and its retention (Figure S16b), with the increase of scan rate was observed. Finally, galvanostatic charge-discharge (GCD) experiments on IEP-27-SR buckypaper electrode were performed to study the rate capability at different current densities in both the selected electrolytes (1 M H<sub>2</sub>SO<sub>4</sub> and 5 M KOH). As seen from Figure 6(a and b), the GCD curves exhibit a sloping profile, with a pair of charging/discharging plateaus around  $-0.35 \text{ V}$  vs. Hg/HgSO<sub>4</sub> (in 1 M H<sub>2</sub>SO<sub>4</sub> electrolyte) and around  $-0.61 \text{ V}$  vs. Hg/HgO (in 5 M KOH electrolyte), agreeing well with the CV profiles. In both the electrolytes, the discharge capacities constantly decrease with increase in the C-rates, but more evidently in the alkaline electrolyte (Figure 6b). For instance, in 1 M H<sub>2</sub>SO<sub>4</sub>, at the fixed C-rate of 2 C ( $1 \text{ C} = 194 \text{ mA g}^{-1}$ ), IEP-27-SR delivers a high specific capacity of  $134 \text{ mAh g}^{-1}$  that decreased to only  $105 \text{ mAh g}^{-1}$  when the C-rate increased to 30 C. Remarkably, IEP-27-SR hybrid still attains an impressively high capacity of  $74 \text{ mAh g}^{-1}$  at the very high C-rate of 180 C, that corresponds to 55% of capacity retention compared to the value at 2 C (Figure 6c). In comparison, in 5 M KOH, the specific capacity at the same rate (2 C) was  $130 \text{ mAh g}^{-1}$  and down-turned to  $72 \text{ mAh g}^{-1}$  at the higher current density of 30 C. These experiments in three-electrode study clearly show the superior electrochemical behaviour of IEP-27-SR in the acidic electrolyte compared to that in the alkaline in terms of high specific capacity and enhanced rate capability owing to the high material activity, higher  $k^0$  and less-diffusion limited redox processes.

## Assembly and electrochemical assessment of AC//IEP-27-SR device

After preliminary electrochemical investigations of IEP-27-SR in the three-electrode configuration, representative two electrode coin cells vs activated carbon (AC) were assembled in order to demonstrate IEP-27-SR availability to construct a device. AC electrodes with a high mass loading of  $30 \text{ mg cm}^{-2}$  were combined with IEP-27-SR to limit the device capacity by the polymer electrode. Once again, choosing 1 M H<sub>2</sub>SO<sub>4</sub> and 5 M KOH as the electrolytes, rate capability and long-term cyclabilities of the assembled AC//IEP-27-SR cell were evaluated.

As shown in Figure 7(a–c), the AC//IEP-27-SR in 1 M H<sub>2</sub>SO<sub>4</sub> exhibits an excellent rate performance when the C-rate is increased from 2 C up to 60 C. At a 2 C rate, the cell shows a high specific capacity of  $168 \text{ mAh g}^{-1}$  and still retains an impressive capacity of  $119 \text{ mAh g}^{-1}$  at 30 C, in the potential window of  $-0.6$ – $+0.3 \text{ V}$  (vs AC; Figure 7a). In the 5 M KOH, the cell attains a reasonably high specific capacity of  $122 \text{ mAh g}^{-1}$  at 2 C and maintains specific capacity of  $66 \text{ mAh g}^{-1}$  at 30 C (Figure 7b, c). When the C-rate was reset to 2 C after rate capability test, the device in 1 M H<sub>2</sub>SO<sub>4</sub> almost recovered to its initial capacity value suggesting superior stability and tolerance towards high currents. However, a small loss of capacity ( $10 \text{ mAh g}^{-1}$ ) was observed in 5 M KOH, probably due to the hindered stability in alkaline medium. But in both the cases, coulombic efficiencies were close to 100% at all the C-rates.

The long-term cycle stability of AC//IEP-27-SR was evaluated by repeated GCD experiments at a representative low and high C-rates of 2 C and 10 C, respectively, in both the selected electrolytes. In 5 M KOH, the cell could reach a high initial capacity of  $136 \text{ mAh g}^{-1}$  at 2 C (Figure S17) that decreased to  $91 \text{ mAh g}^{-1}$  after 600 cycles (capacity retention of 67%) and of  $91 \text{ mAh g}^{-1}$  that reduced to  $45 \text{ mAh g}^{-1}$  after 30000 cycles (capacity retention 50%) at 10 C (Figures 7d and S18a). Moreover, the CE values were  $>99\%$  throughout the cycling experiments in 5 M KOH. Impressively in 1 M H<sub>2</sub>SO<sub>4</sub>, the cell could reach high specific capacity values of  $119$  and  $114 \text{ mAh g}^{-1}$  at 2 C (Figure S19) and 10 C (Figures 7d and S18b), respectively. Although slightly lower CEs in the range of 80%–100% and 93%–96%, at 2 and 10 C, respectively, were

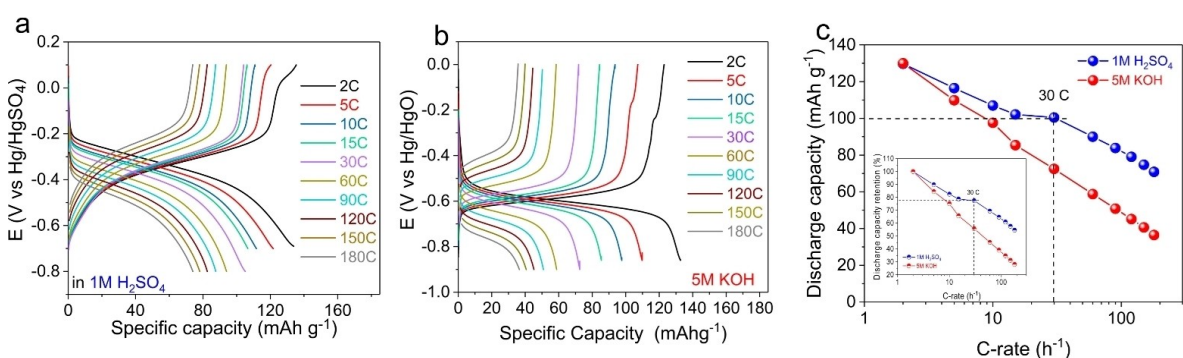


**Figure 6.** Rate capability of IEP-27-SR buckypaper electrodes in 1 M H<sub>2</sub>SO<sub>4</sub> and 5 M KOH evaluated in three-electrode set-up: a, b) specific capacity-potential profiles in a) 1 M H<sub>2</sub>SO<sub>4</sub>, b) 5 M KOH, and c) the corresponding discharge capacities at various C-rates.

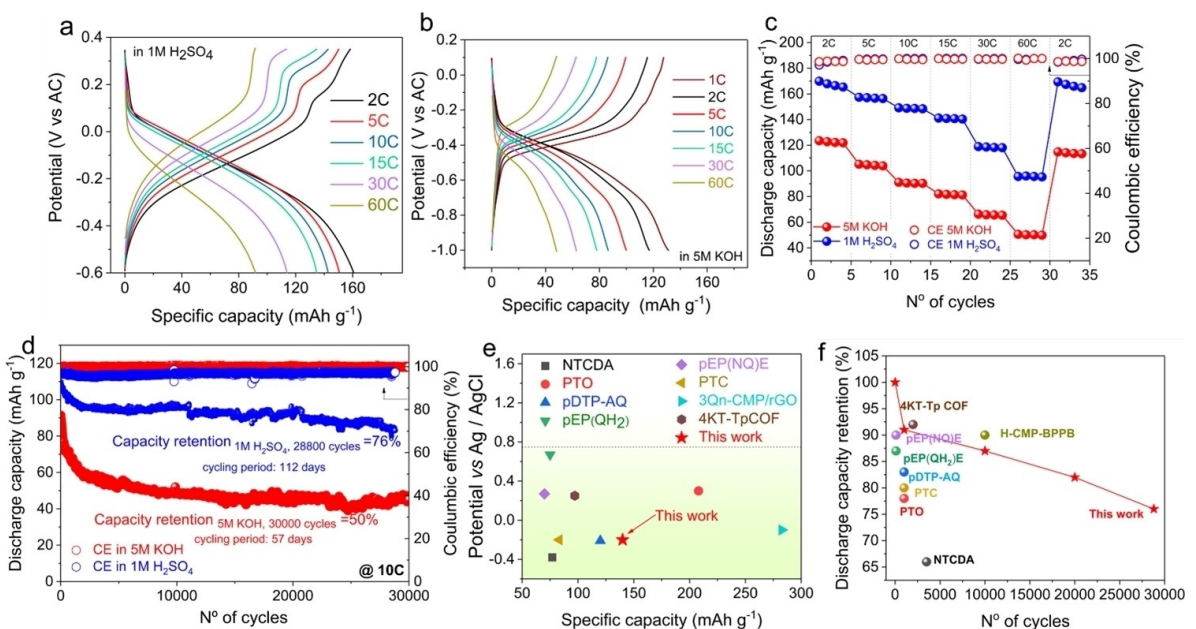


**Figure 7.** Electrochemical performance of IEP-27-SR in 1 M H<sub>2</sub>SO<sub>4</sub> and 5 M KOH evaluated using two electrodes cell against oversized AC. a–c) Rate capability: specific capacity-potential profiles in a) 1 M H<sub>2</sub>SO<sub>4</sub> and b) 5 M KOH, c) discharge capacity vs. cycle number at various C-rates. d) Cycle stability: discharge specific capacity and Coulombic efficiencies measured at 10 C. Comparison of electrochemical performance of IEP-27-SR in terms of e) specific capacity and f) cycle stability in acidic electrolyte with various organic electrode materials reported in literature.

obtained in 1 M H<sub>2</sub>SO<sub>4</sub>, the capacity retention was extraordinary maintained, retaining 100% and 76% of their initial capacities after 4100 and 28800 cycles that correspond to 106 and 112 days of cycling at 2 C (Figure S19) and at 10 C (Figures 7d and S18b), respectively. This indicates that the low CE is not due to parasitic reactions provoking irreversible degradation in the polymer electrode but more probably due to the hydrogen evolution reactions of the electrolyte. This reaction, that might be somehow promoted at low C-rates at the high surface area electrode (Figure S20a), can also be further avoided with the optimization of well-balanced full cell design and slightly reducing the operating voltage (Figure S20b).

Finally, the electrochemical performance of IEP-27-SR in acidic electrolyte is compared with the state-of-the-art literature reports across different classes of organic electrodes, including small organic molecules,<sup>[30–33]</sup> linear<sup>[34–38]</sup> and porous<sup>[39–44]</sup> polymers (see Table S4 in the Supporting Information). As shown in Figure 7e, the maximum attained specific discharge capacity of 168 mAh g<sup>-1</sup> is higher than most of the reported examples, except PTO (208 mAh g<sup>-1</sup>)<sup>[31]</sup> and 3Qn-CMP/rGO (282 mAh g<sup>-1</sup>)<sup>[41]</sup> – the former and latter examples is a small molecule and a porous polymer, respectively. Another stimulating merit of our IEP-27-SR is its outstanding cycling stability. However, comparing the cyclability (capacity retention per cycle) with the reported systems is not straightforward, which depends on many factors, such as cycling rate, mass loading, depth of charge/discharge, temperature, etc. Here, we tried to compare our IEP-27-SR with those tested in similar experimental conditions, for instance at 10 C ( $\approx 2 \text{ A g}^{-1}$ ). Undoubtedly, cycle stability of IEP-27-SR is far superior to the reported small molecules and linear polymers, whatever is the applied current

density for the cyclability test (Figure 7f). Despite an impressive demonstration of the long-term cyclability of porous polymers, 3-OH COF,<sup>[42]</sup> H-CMP-BPPB,<sup>[44]</sup> and 2 KT-Tp COF<sup>[43]</sup> that retained 95% (at  $0.5 \text{ A g}^{-1}$ , 10000 cycles) and 90% (at  $1 \text{ A g}^{-1}$ , 10000 cycles) capacity respectively, longer cycling was not reported. However, notably the capacity/capacitance of these examples, 3-OH COF ( $57 \text{ mF cm}^{-2}$ ), H-CMP-BPPB ( $36 \text{ mAh g}^{-1}$ ), and -Tp COF ( $43 \text{ F g}^{-1}$ ) are par compared to IEP-27-SR. Remarkably, our IEP-27-SR was subjected to much prolonged cycling test over an extended period of 112 days that comprised 28800 cycles at 10 C, which displayed an outstanding 76% capacity retention – one of the best performance, to the best of our knowledge. Thanks to the insolubility and structural robustness of the IEP-27-SR 3D porous structure, rendered an impressive, prolonged cycle stability, particularly in the acid media. In summary, our IEP-27-SR simultaneously achieved high specific capacity, good rate capability and ultra-long cyclability in acidic electrolyte compared to the state-of-the-art literature reports.

## Conclusion

In summary, we reported the successful synthesis, physico-chemical and electrochemical characterization of a new hybrid phenazine-based conjugated porous polymer (IEP-27-SR) and SWCNTs and RGO and its application as versatile ultra-robust organic electrode material in alkaline and acidic electrolytes. Based on electrochemical analyses, supported by DFT calculations, we revealed that phenazine redox units of IEP-27-SR undergo proton-coupled redox reactions in acidic, a mixed

proton/alkali metal cation, probably dominated by protons in neutral, and a mixed proton/alkali metal cation, probably dominated by alkali metal cations in basic electrolytes. Optimistically, the IEP-27-SR exhibited reasonably low discharge potentials of  $-0.35$  V (vs. Hg/HgSO<sub>4</sub>) and  $-0.6$  V (vs. Hg/HgO) with high capacities of 134 and 80 mAh g<sup>-1</sup> in 1 M H<sub>2</sub>SO<sub>4</sub> and 5 M KOH, respectively, evaluated in the standard three-electrode cell, making it as a promising high capacity anode to construct full cells. A representative AC//IEP-27-SR device has also been developed that simultaneously delivered high specific capacity (168 mAh g<sup>-1</sup> at 2 C), impressive rate performance (96 mAh g<sup>-1</sup> at 60 C) and ultra-long cycle stability (76% capacity retention at 10 C over 28800 cycles that last for 112 days) in 1 M H<sub>2</sub>SO<sub>4</sub>. These combined studies at the electrode and device level suggests that IEP-27-SR can be applied as high performance organic anode in different aqueous capacitors and batteries, particularly in acidic energy storage devices, and our current on-going efforts focus on developing such practical proton batteries (e.g., polymer-air, polymer-MnO<sub>2</sub>, etc.).

## Experimental Section

### Materials

Unless noted otherwise, all the reactions were performed using flame-dried glassware under an argon atmosphere using standard Schlenk techniques. 4-bromoaniline (97%, Aldrich), 1-bromo-4-nitrobenzene (99%, Aldrich), potassium *tert*-butoxide (KOtBu;  $\geq 98\%$ , Aldrich), *N,O*-bis(trimethylsilyl)acetamide (98%, abcr), copper (I) iodide (CuI; 98%, Fluorochem), tetrakis (triphenylphosphine) palladium (0) (Pd(PPh<sub>3</sub>)<sub>4</sub>; 99%, abcr), 1,3,5-triethynylbenzene ( $> 98\%$ , abcr), reduced graphene oxide (RGO; Nanografi), single-walled carbon nanotubes (SWCNT; Nanografi), polyvinylidene fluoride (PVDF; Sigma Aldrich), hexadecyltrimethylammonium bromide (CTAB;  $\geq 98\%$ , Sigma Aldrich). Anhydrous tetrahydrofuran (THF), *N,N*-dimethylformamide (DMF) were purchase from Chemlab and used as received. Dichloromethane (CH<sub>2</sub>Cl<sub>2</sub>), ethyl acetate (EtOAc), ethanol (EtOH) and methanol (MeOH) were high-performance liquid chromatography (HPLC) grade, purchase from Chemlab and used without further purification. Silica gel (Fluorochem: 40–63  $\mu$ m) was used as stationary phase for purification of crude reaction mixtures by flash column chromatography. The reactions were monitored with analytical thin-layer chromatography (TLC) silica gel plate (Fluorochem, F254). For the neutral experiments the salts used were potassium chloride (KCl; puriss, Aldrich), sodium chloride (NaCl; 99.8%, Chemlab), lithium chloride (LiCl;  $> 98\%$ , Alfa Aesar).

### Methods

**Synthesis of 2,7-dibromophenazine (2):** 2,7-dibromophenazine was synthesized via a two-step procedure adapted from a previous report<sup>[52]</sup> and the synthetic process is described in detail below.

**Step 1:** To a 250 mL round-bottom flask, potassium *t*-butoxide (9.78 g, 87.198 mmol, 3 equiv.) and THF (110 mL) were added; the solution was cooled to  $-78^{\circ}\text{C}$  (liquid nitrogen/ethyl acetate), and stirred for c.a. 10 min. 4-bromoaniline (5.00 g, 29.07 mmol, 1.00 equiv.) dissolved in THF (30 mL), dried and under argon, was added dropwise via a syringe (c.a. 3 min), followed by 1-bromo-4-

nitrobenzene (5.87 g, 29.07 mmol, 1.00 equiv.) dissolved in THF (30 mL) also added dropwise via a syringe (ca 3 min). The reaction was magnetically stirred at  $-78^{\circ}\text{C}$  for 1 h, while its progress being monitored by TLC. Then, the reaction mixture was poured into a stirring solution of saturated ammonium chloride (350 mL). The product was then extracted with EtOAc (3·150 mL), and the organics were combined, washed with water (3·100 mL) and brine (3·100 mL). The organics were collected, dried with anhydrous magnesium sulphate, filtered, and concentrated onto silica gel. The residue was purified via flash column chromatography using DCM as eluent. The amount of the intermediated obtained as a brown solid was quantitative.

**Step 2:** To a 250 mL round-bottom flask, intermediate (1) (10.2 g 28.49 mmol, 1.00 equiv. assume pure for equiv. calculations), was dissolved in 80 mL of DMF, followed by adding *N,O*-bis(trimethylsilyl)acetamide (35 mL, 142.45 mmol, 5.00 equiv.). The reaction was stirred at room temperature for 41 h. The precipitate was collected via filtration and further washed with cold EtOH ( $\sim$  150 mL) to give a light-yellow solid (4.26 g, 72% yield over two steps).

<sup>1</sup>H NMR (500 MHz, CDCl<sub>3</sub>; ppm):  $\delta = 8.45$  (d,  $J = 2.1$  Hz, 2H; Ar–H), 8.11 (d,  $J = 9.2$  Hz, 2H; Ar–H), 7.92 (dd,  $J = 9.2, 2.1$  Hz, 2H; Ar–H).

<sup>13</sup>C NMR (125 MHz, CDCl<sub>3</sub>):  $\delta = 143.65, 142.35, 135.21, 131.77, 130.93, 125.69$ . IR (cm<sup>-1</sup>):  $\tilde{\nu} = 538$  (C–Br), 715 (C–H oop or C=C arom, C–Br), 807 (C–H oop or C=C arom), 881, 1032 (C–Br), 1123, 1172, 1285, 1343, 1397, 1450, 1498 (C=N), 1606 (C=N), 1767, 1917 (combined bands), 3048 (C–H arom).

Characterization data fit to the compound previously reported.<sup>[52]</sup>

**Synthesis of IEP-27-SR by miniemulsion polymerization and solvothermal approach:** Phenazine-based conjugated microporous polymer SWCNTs+RGO (2.5 + 2.5 wt.% feed w.r.t 2) hybrid was synthesized following a two-step polymerization combining miniemulsion and solvothermal method as previously reported by us.<sup>[51]</sup> First, the ultrasonic dispersion of SWCNTs (8.10 mg) and RGO (8.10 mg) in toluene (8 mL) was obtained with the aid of probe-type tip sonicator for 10 min. Then, 2,7-dibromophenazine (2; 250 mg, 0.74 mmol, 1.5 equiv.) and 1,3,5-triethynylbenzene (74.05 mg, 0.49 mmol, 1 equiv.) dissolved in Et<sub>3</sub>N (8 mL) were added to the aforementioned dispersion under stirring. The resulting suspension was sonicated until the solids were optimally dispersed. After that the aforementioned solution was slowly added to 50 mL of 1% aqueous CTAB solution into a beaker and further homogenized by sonication for 10 min. This reaction mixture was then transferred to a two-necked round bottom flask, and Pd(PPh<sub>3</sub>)<sub>4</sub> (22.8 mg, 0.02 mmol, 0.04 equiv. and CuI (7.51 mg, 0.04 mmol, 0.08 equiv.) were added to the flask; the mixture was degassed by bubbling argon for 15 min and then, stirred vigorously for 3 h under argon atmosphere at  $80^{\circ}\text{C}$ . The miniemulsion dispersion was transferred into a Teflon-lined stainless-steel autoclave and heated to  $150^{\circ}\text{C}$  during 3 h. The crude solids were filtered and washed with a large amount of milli-Q-water, MeOH, THF and CH<sub>2</sub>Cl<sub>2</sub>, in that order, and then dried at  $70^{\circ}\text{C}$  under vacuum overnight. The obtained yield of IEP-27-SR was quantitative ( $> 99\%$ ), with a mass of 231 mg. Based on the gravimetry, the final weight composition of the hybrid was approximately calculated to be 91:3.5:3.5:1:1 (IEP-27:SWCNTs:RGO:Pd:Cu).

### Characterization methods

<sup>1</sup>H and <sup>13</sup>C NMR spectra were recorded at 500 MHz (<sup>1</sup>H NMR), and at 100 MHz (<sup>13</sup>C NMR) using CDCl<sub>3</sub> as solvent with the residual solvent signal as internal reference (CDCl<sub>3</sub> 7.26 and 77.2 ppm). Fourier-transform infrared spectra (FTIR) were recorder on a Nicolet 6700 from Thermo Scientific and are reported in terms of frequency of

absorption ( $\text{cm}^{-1}$ ). The specific surface area and pore-size distribution were determined by  $\text{N}_2$  adsorption–desorption isotherms at 77 K analysis and were carried out using Autosorb iQ2-Quantachrome Instruments. Before analysis, the samples were thoroughly dried and degassed at 100 °C for 10 h to remove the adsorbed gases/moisture. The specific surface area was calculated by two methods; Brunauer, Emmett and Teller equation (BET) ( $S_{\text{BET}}$ ) and total pore volume ( $V_{\text{tot}}$ ), micropore volume ( $V_{\text{micro}}$ ) and microporous and mesoporous surface area ( $S_{\text{micro}}/\text{DFT}$ ,  $S_{\text{meso}}/\text{DFT}$ ) were also determined by Quenched Solid Density Functional Theory (QSDFT) method using a calculation model with slit, cylindrical and sphere pores (SDFT). XRD patterns were recorded by using a PANalytical Empyrean diffractometer with Cu  $\text{K}\alpha$  radiation ( $\lambda = 1.54178 \text{ \AA}$ ) at a scanning rate of 0.2° s. The microscopic features of hybrid IEP-27-SR were carried out using a field-emission scanning electron microscopy (FESEM; Hitachi TM-1000) and transmission electron microscopy (TEM; FEI Talos F200X) imaging techniques. The TEM images were acquired with an electron acceleration energy of 200 kV. The field emission scanning electron microscopy (JEOL JSM-7800F Prime) was used to observe the surface morphology of the samples, with an accelerating voltage of 15 kV.

### Electrode preparation

**Preparation of IEP-27-SR buckypaper electrode.** We prepared IEP-27-SR buckypaper electrodes by dispersing together SWCNTs and IEP-27-SR in NMP and IPA solvents (1:1, v/v), followed by vacuum-assisted filtration processes, as reported in our recent articles.<sup>[50,63]</sup> For instance, a buckypaper with the polymer mass loading of 2 mg  $\text{cm}^{-2}$  is prepared as following: 17 mg of IEP-27-SR and 3 mg of SWCNTs (80/20 wt.%) were added to 7 mL of NMP and 7 mL of IPA and dispersed by tip sonication for 10 min. After being stirred overnight at room temperature, the ink was sonicated for 1 h in a bath sonicator (Branson 2510, 100 W, 42 kHz). The suspension was filtrated through a Nylon filter (45 mm diameter, pore size ~0.45  $\mu\text{m}$ ) with the aid of vacuum, followed by thorough rinsing with IPA to remove loosely bound polymer. The buckypaper was carefully peeled off from the filter and dried overnight at 75 °C under vacuum. This composite electrode is a polymer-supported, self-standing, metal current collector- and binder-free buckypaper. The buckypaper electrodes were cut into circular discs with a diameter of 8 mm.

**Preparation of over-capacitive activated carbon (AC) counter electrode.** Activated carbon, carbon black, nafton, polyvinylidene fluoride (70/10/5/15 wt/wt%) were grinded together and adding NMP until a smooth slurry was formed. The slurry was then mixed in an ultra turrax homogenizer, followed by application of light vacuum to remove trapped bubbles, before proceeding to electrode casting. This slurry was applied onto carbon cloth with a mass loading of approximately 30 mg  $\text{cm}^{-2}$  using doctor blading device and dried overnight at 80 °C under vacuum. At least 3-fold capacity excess was maintained to make sure that the cell capacity is limited by the anode.

### Preparation of coin cells

A coin-type (LIR2032) electrochemical half-cell was fabricated by assembling an AC as a counter and reference electrodes, porous Whatman® glass microfiber filters (Grade GF/B) as separator soaked with ~200  $\mu\text{L}$  of electrolyte and a circular disc (8 mm) of buckypaper composite working electrode, in a high-purity argon filled glovebox (MBraun) to avoid any possible contamination by oxygen. The aqueous electrolytes were prepared by dissolving KOH, LiOH, NaOH,  $\text{H}_2\text{SO}_4$ , NaCl, LiTFSI, KCl in degassed milli-Q water.

### Electrochemical measurements

Cyclic voltammetry (CV) profiles of IEP-27-SR were obtained using a flooded three-electrode electrochemical cell with polymer deposited on glassy carbon (GC; for pH-dependency study) or using buckypaper electrode clamped with a holder and Pt wire as the working and counter electrode, respectively. When the electrolytes were basic and acidic, respectively, Hg/HgO and Hg/HgSO<sub>4</sub> served as reference electrodes. For the pH-dependency study, we selected Ag/AgCl as the reference electrode. Britton-Robinson aqueous universal buffer solutions of various pH values were prepared by mixing appropriate volumes of acids and basic buffer components.<sup>[64]</sup> The acidic buffer component comprises 1 M phosphoric acid, 1 M boric acid, and 1 M acetic acid. The basic buffer component is 5 M sodium hydroxide solution. The electrode inks were prepared by dispersing IEP-27-SR with RGO and PVDF in NMP. The ink was then uniformly deposited on a masked GC, and dried under vacuum to remove the solvent. The composition of the modified GC working electrode is 80:10:10 (IEP-27-SR:SWCNT:PVDF in NMP). The electrolyte was degassed with argon, and voltammograms were recorded at room temperature under a positive pressure of argon atmosphere. The CV and GCD in three-electrode experiments were performed with a Bio-logic VMP3 multichannel Potentiostat/Galvanostat (Biologic SP-150). As a commonly used procedure for polymer-based organic batteries, the specific capacities and current rates (C-rates) were normalized with respect to the mass of polymer in the electrode. The cycling and rate performance of coin cells were evaluated by GCD experiments with a Neware battery cycler at room temperature.

### Supporting Information

Supporting table, computational procedure and figures are in Supporting Information.

Supporting Information is available from the Wiley Online Library or from the author.

### Acknowledgements

Authors thank the European Union's Horizon 2020 research and innovation programme under the Marie Skłodowska-Curie Grant agreement (Grant No 860403) and Spanish Government; MCIN/AEI/10.13039/501100011033/FEDER "A way of making Europe" (PID2021-124974OB-C21 and PID2019-106315RB-I00) for the funding. N. P. appreciates fellowship IJC2020-043076-I-I funded by MCIN/AEI/0.13039/501100011033 and by the European Union NextGenerationEU/PRTR. A. M. thanks the TALENTO grant (2021-5 A/AMB-20946) from Comunidad de Madrid for financial support, and acknowledges the computing facilities of CSUC for providing resources that contributed to the research results reported within this paper.

### Conflict of Interest

The authors declare no conflict of interest.

## Data Availability Statement

Data will be in a public repository that issues datasets with DOI if the manuscript is accepted for publication.

**Keywords:** acidic electrolyte · alkaline electrolyte · conjugated microporous polymer · organic electrode material · phenazine polymer

- [1] J. B. Goodenough, *Energy Storage Mater.* **2015**, *1*, 158–161.  
[2] J. B. Goodenough, *Energy Environ. Sci.* **2013**, *7*, 14–18.  
[3] Z. Song, H. Zhou, *Energy Environ. Sci.* **2013**, *6*, 2280–2301.  
[4] A. Ponrouch, J. Bitenc, R. Dominiko, N. Lindahl, P. Johansson, M. R. Palacin, *Energy Storage Mater.* **2019**, *20*, 253–262.  
[5] A. R. Shekhar, M. H. Parekh, V. G. Pol, *J. Power Sources* **2022**, *523*, 231015.  
[6] C. P. Grey, J. M. Tarascon, *Nat. Mater.* **2017**, *16*, 45–56.  
[7] J. Kalhoff, G. G. Eshetu, D. Bresser, S. Passerini, *ChemSusChem* **2015**, *8*, 2154–2175.  
[8] Y. Liang, Y. Yao, *Nat. Rev. Mater.* **2023**, *8*, 109–122.  
[9] T. Liu, X. Cheng, H. Yu, H. Zhu, N. Peng, R. Zheng, J. Zhang, M. Shui, Y. Cui, J. Shu, *Energy Storage Mater.* **2019**, *18*, 68–91.  
[10] J. Liu, C. Xu, Z. Chen, S. Ni, Z. X. Shen, *Green Energy & Environ.* **2018**, *3*, 20–41.  
[11] J. B. Goodenough, A. Manthiram, *MRS Commun.* **2014**, *4*, 135–142.  
[12] J. Huang, Z. Guo, Y. Ma, D. Bin, Y. Wang, Y. Xia, *Small Methods* **2019**, *3*, 1–20.  
[13] N. Goujon, N. Casado, N. Patil, R. Marcilla, D. Mecerreyres, *Prog. Polym. Sci.* **2021**, *122*, 101449.  
[14] C. Han, J. Zhu, C. Zhi, H. Li, *J. Mater. Chem. A* **2020**, *8*, 15479–15512.  
[15] N. Patil, A. Mavrandonakis, C. Jérôme, C. Detrembleur, J. Palma, R. Marcilla, *ACS Appl. Energ. Mater.* **2019**, *2*, 3035–3041.  
[16] G. Liang, F. Mo, X. Ji, C. Zhi, *Nat. Rev. Mater.* **2020**, *6*, 109–123.  
[17] K. Hatakeyama-Sato, H. Wakamatsu, R. Katagiri, K. Oyaizu, H. Nishide, *Adv. Mater.* **2018**, *30*, 1800900.  
[18] Y. Liang, Y. Jing, S. Ghetyani, K.-Y. Lee, P. Liu, A. Facchetti, Y. Yao, *Nat. Mater.* **2017**, *16*, 841–848.  
[19] E. I. Romadina, A. V. Akkuratov, O. Simoska, K. J. Stevenson, *Batteries* **2022**, *8*, 288.  
[20] J. Li, H. Yan, C. Xu, Y. Liu, X. Zhang, M. Xia, L. Zhang, J. Shu, *Nano Energy* **2021**, *89*, 106400.  
[21] R. J. Gilliam, J. W. Graydon, D. W. Kirk, S. J. Thorpe, *Int. J. Hydrogen Energy* **2007**, *32*, 359–364.  
[22] Y. Li, L. Liu, C. Liu, Y. Lu, R. Shi, F. Li, J. Chen, *CHEMPR* **2019**, *5*, 2159–2170.  
[23] A. Pendashteh, J. S. Sanchez, J. Palma, M. Anderson, R. Marcilla, *Energy Storage Mater.* **2019**, *20*, 216–224.  
[24] L. Zhong, Z. Fang, C. Shu, C. Mo, X. Chen, D. Yu, *Angew. Chem. Int. Ed.* **2021**, *60*, 10164–10171; *Angew. Chem.* **2021**, *133*, 10252–10259.  
[25] N. Wang, H. Wan, J. Duan, X. Wang, L. Tao, J. Zhang, H. Wang, *Mater. Today* **2021**, *11*, 100149.  
[26] T.-K. Ying, X.-P. Gao, W.-K. Hu, F. Wu, D. Noréus, *Int. J. Hydrogen Energy* **2006**, *31*, 525–530.  
[27] S. R. Ovshinsky, M. A. Fetcenko, J. Ross, *Science* **1993**, *260*, 176–181.  
[28] T. Tomai, S. Mitani, D. Komatsu, Y. Kawaguchi, I. Honma, *Sci. Rep.* **2014**, *4*, 1–6.  
[29] M. Shi, J. He, Y. Zhao, L. Zhao, K. Dai, C. Yan, *Mater. Des.* **2022**, *222*, 111043.  
[30] W. Han, M. Li, Y. Ma, J. Yang, *Electrochim. Acta* **2022**, *403*, 139550.  
[31] Z. Guo, J. Huang, X. Dong, Y. Xia, L. Yan, Z. Wang, Y. Wang, *Nat. Commun.* **2020**, *11*, 959.  
[32] Y. Zhang, Y. An, L. Wu, H. Chen, Z. Li, H. Dou, V. Murugadoss, J. Fan, X. Zhang, X. Mai, Z. Guo, *J. Mater. Chem. A* **2019**, *7*, 19668–19675.  
[33] J. Yang, H. Wang, Y. Yang, J. Wu, P. Hu, L. Guo, *Nanoscale* **2017**, *9*, 9879–9885.  
[34] N. Kurra, R. Wang, H. N. Alshareef, *J. Mater. Chem. A* **2015**, *3*, 7368–7374.  
[35] H. Wei, H. Gu, J. Guo, S. Wei, Z. Guo, *J. Electrochem. Soc.* **2013**, *160*, G3038–G3045.  
[36] X. Wang, J. Zhou, W. Tang, *Energy Storage Mater.* **2021**, *36*, 1–9.  
[37] C. Strietzel, M. Sterby, H. Huang, M. Strømme, R. Emanuelsson, M. Sjödin, *Angew. Chem. Int. Ed.* **2020**, *59*, 9631–9638; *Angew. Chem.* **2020**, *132*, 9718–9725.  
[38] M. Zhu, L. Zhao, Q. Ran, Y. Zhang, R. Peng, G. Lu, X. Jia, D. Chao, C. Wang, *Adv. Sci.* **2022**, *9*, 2103896.  
[39] S. Kandambeth, J. Jia, H. Wu, V. S. Kale, P. T. Parvatkar, J. Czaban-Józwik, S. Zhou, X. Xu, Z. O. Ameur, E. Abou-Hamad, A. H. Emwas, O. Shekhhah, H. N. Alshareef, M. Eddaoudi, *Adv. Energy Mater.* **2020**, *10*, 2001673, DOI 10.1002/aenm.202001673.  
[40] C. R. Mulzer, L. Shen, R. P. Bisbey, J. R. McKone, N. Zhang, H. D. Abruna, W. R. Dichtel, *ACS Cent. Sci.* **2016**, *2*, 667–673.  
[41] D. Fang, X. Wang, S. Zhang, L. Sheng, J. Tang, J. Zhou, W. Tang, *Sci. China Mater.* **2021**, *65*, 958–966.  
[42] S. Haldar, R. Kushwaha, R. Maity, R. Vaidhyanathan, *ACS Materials Lett.* **2019**, *1*, 490–497.  
[43] M. Li, J. Liu, Y. Li, G. Xing, X. Yu, C. Peng, L. Chen, *CCS Chem.* **2021**, *3*, 696–706.  
[44] J. Choi, J. H. Ko, C. W. Kang, S. M. Lee, H. J. Kim, Y. J. Ko, M. Yang, S. U. Son, *J. Mater. Chem. A* **2018**, *6*, 6233–6237.  
[45] Y. Lin, H. Cui, C. Liu, R. Li, S. Wang, G. Qu, Z. Wei, Y. Yang, Y. Wang, Z. Tang, H. Li, H. Zhang, C. Zhi, H. Lv, *Angew. Chemie Int. Ed.* **2023**, *135*, e202218745.  
[46] Z. Wu, P. Yang, S. Wang, S. Li, S. Zhang, *Trends Chem.* **2022**, *4*, 1121–1134.  
[47] S. M. Zeng, X. X. Huang, Y. J. Ma, L. J. Zhi, *New. Carbon. Mater.* **2021**, *36*, 1–18.  
[48] Y. Tong, X. Wang, Y. Zhang, W. Huang, *Inorg. Chem. Front.* **2021**, *8*, 558–571.  
[49] A. Molina, N. Patil, E. Ventosa, M. Liras, J. Palma, R. Marcilla, A. Molina, N. Patil, E. Ventosa, J. Palma, R. Marcilla, M. Liras, *Adv. Funct. Mater.* **2020**, *30*, 1908074.  
[50] R. Grieco, A. Molina, J. S. Sanchez, N. Patil, M. Liras, R. Marcilla, *Mater. Today Energy* **2022**, *27*, 101014.  
[51] A. Molina, N. Patil, E. Ventosa, M. Liras, J. Palma, R. Marcilla, *ACS Energy Lett.* **2020**, *5*, 2945–2953.  
[52] E. Vitaku, C. N. Gannett, K. L. Carpenter, L. Shen, H. D. Abruna, W. R. Dichtel, *J. Am. Chem. Soc.* **2020**, *142*, 16–20.  
[53] A. H. Shah, W. Zaid, A. Shah, U. A. Rana, H. Hussain, M. N. Ashiq, R. Qureshi, A. Badshah, M. A. Zia, H.-B. Kraatz, *J. Electrochem. Soc.* **2015**, *162*, H115–H123.  
[54] L. Li, L. Chen, Y. Wen, T. Xiong, H. Xu, W. Zhang, G. Cao, Y. Yang, L. Mai, H. Zhang, *J. Mater. Chem. A* **2020**, *8*, 26013–26022.  
[55] N. Oyama, T. Ohnsaka, K. Chiba, K. Takahashi, *Bull. Chem. Soc. Jpn.* **1988**, *61*, 1095–1101.  
[56] S. R. Sivakkumar, R. Saraswathi, *J. Appl. Electrochem.* **2004**, *34*, 1147–1152.  
[57] M. Jayalakshmi, M. Mohan Rao, F. Scholz, *Langmuir* **2003**, *19*, 8403–8408.  
[58] N. Patil, A. Mavrandonakis, C. Jérôme, C. Detrembleur, J. Palma, R. Marcilla, *ACS Appl. Energ. Mater.* **2019**, *2*, 3035–3041.  
[59] T. Sun, C. Liu, J. Wang, Q. Nian, Y. Feng, Y. Zhang, Z. Tao, J. Chen, *Nano Res.* **2020**, *13*, 676–683.  
[60] Y. Ji, M.-A. Goulet, D. A. Pollack, D. G. Kwabi, S. Jin, D. De Porcellinis, E. F. Kerr, R. G. Gordon, M. J. Aziz, Y. Ji, E. F. Kerr, R. G. Gordon, M. Goulet, D. G. Kwabi, S. Jin, D. De Porcellinis, M. J. Aziz, Harvard John A Paulson, D. A. Pollack, *Adv. Energy Mater.* **2019**, *9*, 1900039.  
[61] Bard Allen J, Faulkner Larry R, *Electrochemical Methods: Fundamentals and Applications*, 2nd Edition, Wiley, 2008.  
[62] N. Patil, C. de la Cruz, D. Ciurdac, A. Mavrandonakis, J. Palma, R. Marcilla, *Adv. Energy Mater.* **2021**, *11*, 2100939.  
[63] N. Patil, J. Palma, R. Marcilla, *Polymers (Basel)* **2021**, *13*, 1673.  
[64] H. T. S. Britton, R. A. Robinson, *J. Chem. Soc.* **1931**, 1456–1462.

Manuscript received: January 17, 2023

Revised manuscript received: March 10, 2023

Accepted manuscript online: March 27, 2023

Version of record online: April 14, 2023